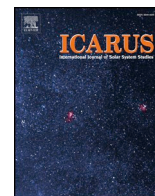




ELSEVIER

Contents lists available at ScienceDirect

Icarus

journal homepage: www.elsevier.com/locate/icarus

Seasonal evolution of temperatures in Titan's lower stratosphere

M. Sylvestre^{a,*}, N.A. Teanby^a, J. Vatant d'Ollone^b, S. Vinatier^c, B. Bézard^c, S. Lebonnois^b, P.G.J. Irwin^d

^a School of Earth Sciences, University of Bristol, Wills Memorial Building, Queens Road, Bristol BS8 1 RJ, UK

^b Laboratoire de Météorologie Dynamique (LMD/IPSL), Sorbonne Université, ENS, PSL Research University, Ecole Polytechnique, Université Paris Saclay, CNRS, 4 Place Jussieu, F 75252 Paris Cedex 05, France

^c LESIA, Observatoire de Paris, Université PSL, CNRS, Sorbonne Université, Univ. Paris Diderot, Sorbonne Paris Cité, 5 place Jules Janssen, Meudon 92195, France

^d Atmospheric, Oceanic, & Planetary Physics, Department of Physics, University of Oxford, Clarendon Laboratory, Parks Road, Oxford OX1 3PU, UK

A B S T R A C T

The Cassini mission offered us the opportunity to monitor the seasonal evolution of Titan's atmosphere from 2004 to 2017, i.e. half a Titan year. The lower part of the stratosphere (pressures greater than 10 mbar) is a region of particular interest as there are few available temperature measurements, and because its thermal response to the seasonal and meridional insolation variations undergone by Titan remain poorly known. In this study, we measure temperatures in Titan's lower stratosphere between 6 mbar and 25 mbar using Cassini/CIRS spectra covering the whole duration of the mission (from 2004 to 2017) and the whole latitude range. We can thus characterize the meridional distribution of temperatures in Titan's lower stratosphere, and how it evolves from northern winter (2004) to summer solstice (2017). Our measurements show that Titan's lower stratosphere undergoes significant seasonal changes, especially at the South pole, where temperature decreases by 19 K at 15 mbar in 4 years.

1. Introduction

Titan has a dense atmosphere, composed of N₂ and CH₄, and many trace gases such as hydrocarbons (e.g. C₂H₆, C₂H₂) and nitriles (e.g. HCN, HC₃N) produced by its rich photochemistry. Like Earth, Titan has a stratosphere, located between 50 km (~ 100 mbar) and 400 km (~ 0.01 mbar), characterized by the increase of its temperature with altitude because of the absorption of incoming sunlight by methane and hazes. Titan's atmosphere undergoes strong variations of insolation, due to its obliquity (26.7°) and to the eccentricity of Saturn's orbit around the Sun (0.0565).

The Cassini spacecraft monitored Titan's atmosphere during 13 years (from 2004 to 2017), from northern winter to summer solstice. Its data are a unique opportunity to study the seasonal evolution of its stratosphere, especially with mid-IR observations from Cassini/CIRS (Composite InfraRed Spectrometer, [Flasar et al., 2004](#)). They showed that at pressures lower than 5 mbar, the stratosphere exhibits strong seasonal variations of temperature and composition related to changes in atmospheric dynamics and radiative processes. For instance, during northern winter (2004–2008), high northern latitudes were enriched in photochemical products such as HCN or C₄H₂, while there was a “hot spot” in the upper stratosphere and mesosphere (0.1–0.001 mbar, [Achterberg et al., 2008](#); [Coustenis et al., 2007](#); [Teanby et al., 2007](#); [Vinatier et al., 2007](#)). These observations were interpreted as evidence

of subsidence above the North Pole during winter, which is a part of the pole-to-pole atmospheric circulation cell predicted for solstices by Titan GCMs (Global Climate Models, [Lora et al., 2015](#); [Lebonnois et al., 2012](#); [Newman et al., 2011](#)). These models also predict that the circulation pattern should reverse around equinoxes, via a transitional state with two equator-to-pole cells. These changes began to affect the South Pole in 2010, when measurements showed that pressures inferior to 0.03 mbar exhibited an enrichment in gases such as HCN and C₂H₂, which propagated downward during autumn, consistent with the apparition of a new circulation cell with subsidence above the South Pole ([Teanby et al., 2017](#); [Vinatier et al., 2015](#)).

Some uncertainties remain about the seasonal evolution of the lower part of the stratosphere, i.e. at pressures from 5 mbar (120 km) to 100 mbar (tropopause, 50 km). Different estimates of radiative time-scales have been calculated for this region. In [Strobel et al. \(2010\)](#), the radiative timescales in this region vary from 0.2 Titan years at 5 mbar to 2.5 Titan years at 100 mbar. This means that the lower stratosphere should be the transition zone from parts of the atmosphere which are sensitive to seasonal insolation variations, to parts of the atmosphere which are not. In contrast, in the radiative-dynamical model of [Bézard et al. \(2018\)](#), radiative timescales are between 0.02 Titan year at 5 mbar and 0.26 Titan year at 100 mbar, implying that this whole region should exhibit a response to the seasonal cycle.

From northern winter to equinox, CIRS mid-IR observations showed

* Corresponding author.

E-mail address: melody.sylvestre@bristol.ac.uk (M. Sylvestre).

<https://doi.org/10.1016/j.icarus.2019.02.003>

Received 11 July 2018; Received in revised form 30 January 2019; Accepted 1 February 2019

Available online 20 February 2019

0019-1035/ © 2019 Elsevier Inc. All rights reserved.

that temperature variations were lower than 5 K between 5 mbar and 10 mbar (Bampasidis et al., 2012; Achterberg et al., 2011). Temporal variations intensified after spring equinox, as Coustenis et al. (2016) measured a cooling by 16 K and an increase in gases abundances at 70°S from 2010 to 2014, at 10 mbar, associated with the autumn subsidence above the South pole. Sylvestre et al. (2018) showed that this subsidence affects pressure levels as low as 15 mbar as they measured strong enrichments in C₂N₂, C₃H₄, and C₄H₂ at high southern latitudes from 2012 to 2016 with CIRS far-IR observations. However, we have little information on temperatures and their seasonal evolution for pressures greater than 10 mbar. Temperatures from the surface to 0.1 mbar can be measured by Cassini radio-occultations, but the published profiles were measured mainly in 2006 and 2007 (Schinder et al., 2011, 2012), so they provide little information on seasonal variations of temperature.

In this study, we analyse all the available far-IR Cassini/CIRS observations to probe temperatures from 6 mbar to 25 mbar, and measure the seasonal variations of lower stratospheric temperatures. As these data were acquired throughout the Cassini mission from 2004 to 2017, and cover the whole latitude range, they provide a unique overview of the thermal evolution of the lower stratosphere from northern winter to summer solstice, and a better understanding of the radiative and dynamical processes at play in this part of Titan's atmosphere.

2. Data analysis

2.1. Observations

We measure lower stratospheric temperatures using Cassini/CIRS (Flasar et al., 2004) spectra. CIRS is a thermal infrared spectrometer with three focal planes operating in three different spectral domains: 10 - 600 cm⁻¹ (17 - 1000 μm) for FP1, 600 - 1100 cm⁻¹ (9 - 17 μm) for FP3, and 1100 - 1400 cm⁻¹ (7 - 9 μm) for FP4. FP1 has a single circular detector with an angular field of view of 3.9 mrad, which has an approximately Gaussian spatial response with a FWHM of 2.5 mrad. FP3 and FP4 are each composed of a linear array of ten detectors. Each of these detectors has an angular field of view of 0.273 mrad.

In this study, we use FP1 far-IR observations, where nadir spectra are measured at a resolution of 0.5 cm⁻¹, in "sit-and-stare" geometry (i.e the FP1 detector probes the same latitude and longitude during the whole duration of the acquisition). In this type of observation, the average spatial field of view is 20° in latitude. An acquisition lasts between 1h30 and 4h30, allowing the recording of 100 to 330 spectra. The spectra from the same acquisition are averaged together, which increases the S/N by a factor \sqrt{N} (where N is the number of spectra). As a result, we obtain an average spectrum where the rotational lines of CH₄ (between 70 cm⁻¹ and 170 cm⁻¹) are resolved and can be used to retrieve Titan's lower stratospheric temperature. An example averaged spectrum is shown in Fig. 1.

We analysed all the available observations with the characteristics mentioned above. As shown in Table 1, this type of nadir far-IR observation has been performed throughout the Cassini mission (from 2004 to 2017), at all latitudes. Hence, the analysis of this dataset enables us to get an overview of Titan's lower stratosphere and its seasonal evolution.

2.2. Retrieval method

We follow the same method as Sylvestre et al. (2018). We use the portion of the spectrum between 70 cm⁻¹ and 400 cm⁻¹, where the main spectral features are: the ten rotational lines of CH₄ (between 70 cm⁻¹ and 170 cm⁻¹), the C₄H₂ band at 220 cm⁻¹, the C₂N₂ band at 234 cm⁻¹, and the C₃H₄ band at 327 cm⁻¹ (see Fig. 1). The continuum emission comes from the collisions between the three main components of Titan's atmosphere (N₂, CH₄, and H₂), and from the spectral contributions of the hazes.

We retrieve the temperature profile using the constrained non-linear inversion code NEMESIS (Irwin et al., 2008). We define a reference atmosphere, which takes into account the abundances of the main constituents of Titan's atmosphere measured by Cassini/CIRS (Coustenis et al., 2016; Nixon et al., 2012; Cottini et al., 2012; Teanby et al., 2009), Cassini/VIMS (Maltagliati et al., 2015), ALMA (Molter et al., 2016) and Huygens/GCMS (Niemann et al., 2010). We also consider the haze distribution and properties measured in previous studies with Cassini/CIRS (de Kok et al., 2007, 2010; Vinatier et al., 2012), and Huygens/GCMS (Tomasko et al., 2008). We consider four types of hazes, following de Kok et al. (2007): hazes 0 (70 cm⁻¹ to 400 cm⁻¹), A (centred at 140 cm⁻¹), B (centred at 220 cm⁻¹) and C (centred at 190 cm⁻¹). For the spectra measured at high northern and southern latitudes during autumn and winter, we add an offset from 1 to 3 cm⁻¹ to the nominal haze B cross-sections between 190 cm⁻¹ and 240 cm⁻¹, as in Sylvestre et al. (2018). This modification improves the fit of the continuum in the "haystack" which is a strong emission feature between 190 cm⁻¹ and 240 cm⁻¹ (see Fig. 1) seen at high latitudes during autumn and winter (e.g. in Coustenis et al., 1999; de Kok et al., 2007; Anderson et al., 2012; Jennings et al., 2012, 2015). The variation of the offset allows us to take into account the evolution of the shape of this feature throughout autumn and winter. The composition of our reference atmosphere and the spectroscopic parameters adopted for its constituents are fully detailed in Sylvestre et al. (2018).

We retrieve the temperature profile and scale factors applied to the *a priori* profiles of C₂N₂, C₄H₂, C₃H₄, and hazes 0, A, B and C, from the spectra using the constrained non-linear inversion code NEMESIS (Irwin et al., 2008). This code generates synthetic spectra from the reference atmosphere. At each iteration, the difference between the synthetic and the measured spectra is used to modify the profile of the retrieved variables, and minimise a cost function, in order to find the best fit for the measured spectrum.

The sensitivity of the spectra to the temperature can be measured with the inversion kernels for the temperature (defined as $K_{ij} = \frac{\partial I_i}{\partial T_j}$, where I_i is the radiance measured at wavenumber w_i , and T_j the temperature at pressure level p_j) for several wavenumbers. The contribution of the methane lines to the temperature measurement can be isolated by defining their own inversion kernels $K_{ij}^{CH_4}$ as follows:

$$K_{ij}^{CH_4} = K_{ij} - K_{ij}^{cont} \quad (1)$$

where K_{ij}^{cont} is the inversion kernel of the continuum for the same wavenumber. Fig. 2 shows $K_{ij}^{CH_4}$ for three of the rotational methane lines in the left panel, and the comparison between the sum of the 10 $K_{ij}^{CH_4}$ (for the 10 rotational CH₄ lines) and inversion kernels for the continuum (K_{ij}^{cont} at the wavenumbers of the CH₄ lines and K_{ij} outside of the CH₄ lines) in the right panel. The CH₄ lines allow us to measure lower stratospheric temperatures generally between 6 mbar and 25 mbar, with a maximal sensitivity at 15 mbar. The continuum emission mainly probes temperatures at higher pressures, around the tropopause and in the troposphere. The continuum emission mostly originates from the N₂-N₂ and N₂-CH₄ collisions induced absorption with some contribution from the hazes, for which we have limited constraints. However, Fig. 2 shows that the continuum emission comes from pressure levels located several scale heights below the region probed by the CH₄ lines, so the lack of constraints on the hazes and tropospheric temperatures does not affect the lower stratospheric temperatures which are the main focus of this study.

2.3. Error sources

The main error sources in our temperature retrievals are the measurement noise and the uncertainties related to the retrieval process such as forward modeling errors or the smoothing of the temperature profile. The total error on the temperature retrieval is estimated by NEMESIS and is in the order of 2 K from 6 mbar to 25 mbar.

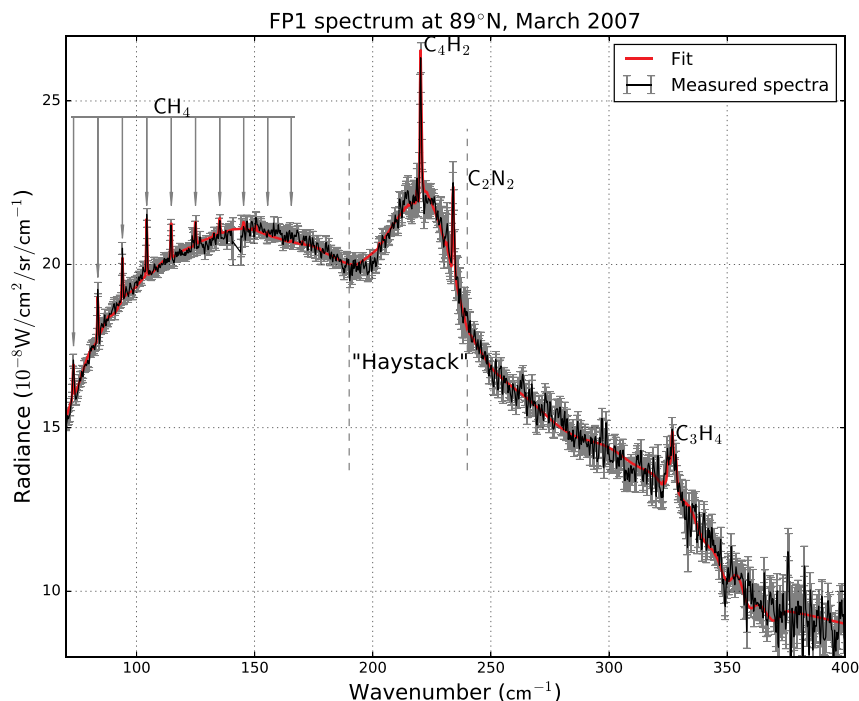


Fig. 1. Example of average spectrum measured with the FP1 detector of Cassini/CIRS (in black) and its fit by NEMESIS (in red). The measured spectrum was obtained after averaging 106 spectra observed at 89°N in March 2007. The rotational lines of CH₄ are used to retrieve stratospheric temperature. The “haystack” feature is visible only at high latitudes during autumn and winter. (For interpretation of the references to color in this figure legend, the reader is referred to the web version of this article.)

The other possible error source is the uncertainty on CH₄ abundance, as Lellouch et al. (2014) showed that it can vary from 1% to 1.5% at 15 mbar. We performed additional temperature retrievals on several datasets, in order to assess the effects of these variations on the temperature retrievals. First, we selected datasets for which CH₄ abundance was measured by Lellouch et al. (2014). In Fig. 3, we show

examples of these tests for two of these datasets: 52°N in May 2007 and 15°S in October 2006, for which Lellouch et al. (2014) measured respective CH₄ abundances of $q_{CH_4} = 1.20 \pm 0.15\%$ and $q_{CH_4} = 0.95 \pm 0.08\%$ (the nominal value for our retrievals is $q_{CH_4} = 1.48 \pm 0.09\%$ from Niemann et al. (2010)). At 52°N, the temperature profile obtained with the methane abundance from Lellouch

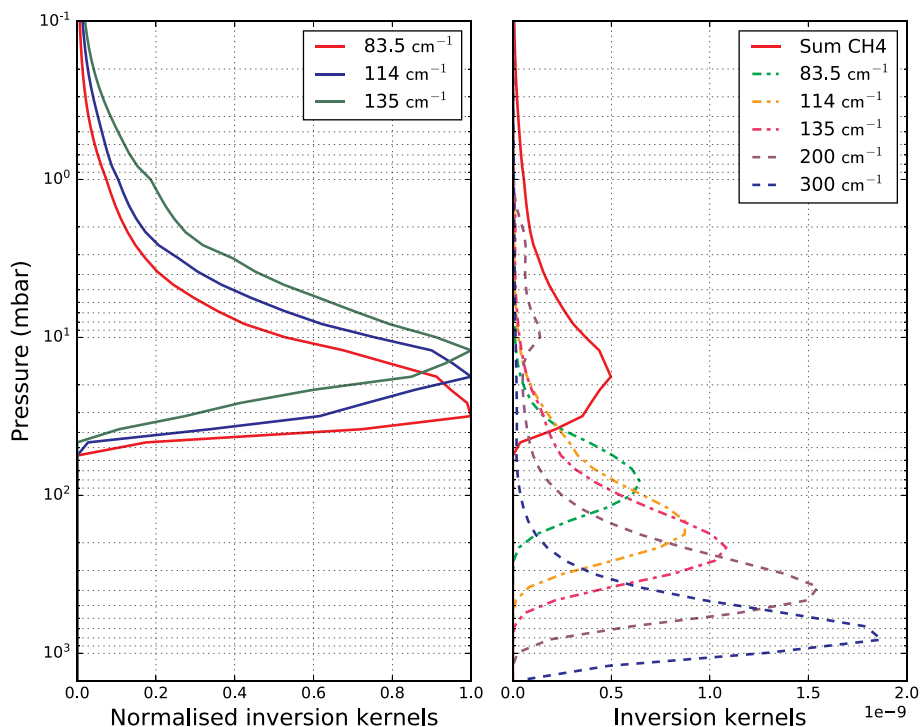


Fig. 2. Sensitivity of temperature measurements at 72°N in April 2007. *Left panel:* Normalized inversion kernels $K_{ij}^{CH_4}$ in three of the CH₄ rotational lines. *Right panel:* Comparison between the inversion kernels in the continuum (K_{ij}^{cont} for three of the CH₄ lines in dot-dashed lines, and K_{ij} for other wavenumbers in the continuum in dashed lines) and the sum of the inversion kernels $K_{ij}^{CH_4}$ of the CH₄ rotational lines. CH₄ rotational lines dominate the temperature retrievals in the lower stratosphere, generally from 6 to 25 mbar (and up to 35 mbar, depending on the datasets). The continuum emission probes temperatures at pressures higher than 50 mbar, mainly in the troposphere.

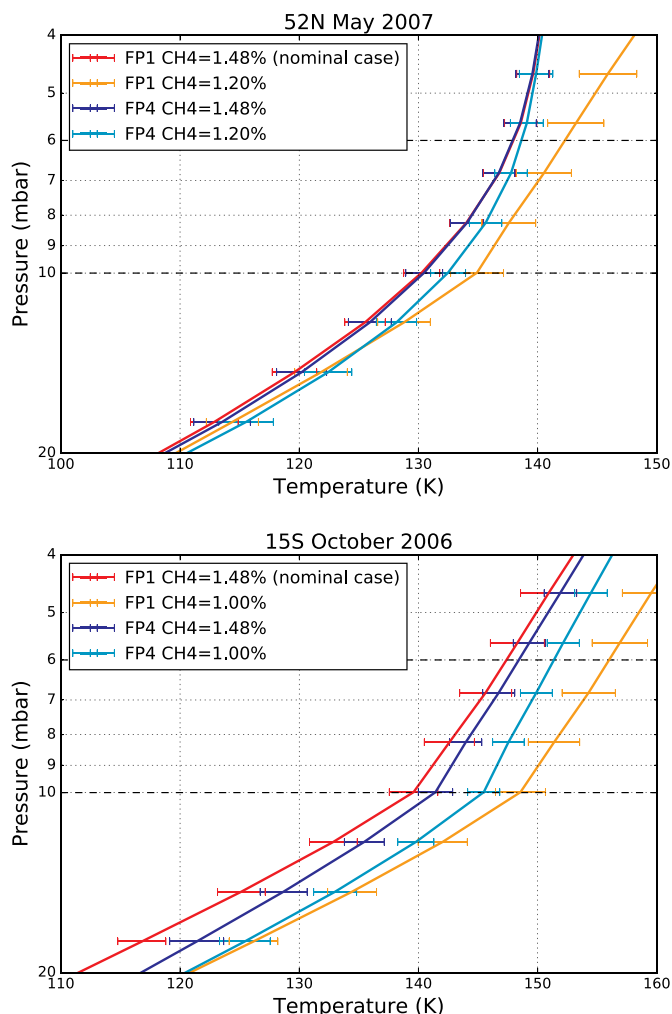


Fig. 3. Temperature profiles from CIRS FP1 and FP4 nadir observations at 52°N in May 2007 (top panel) and 15°S in October 2006 (bottom panel), retrieved with the methane abundances measured by Niemann et al. (2010) (nominal value in this study) and Lellouch et al. (2014). In both cases, the nominal value from Niemann et al. (2010) yields a better agreement between the two types of observations.

et al. (2014) does not differ by more than 4 K from the nominal temperature profile. At 15 mbar (where the sensitivity to temperature is maximal in our retrievals), the difference of temperature between these two profiles is 2 K. Even a CH₄ volume mixing ratio as low as 1% yields a temperature only 4 K warmer than the nominal temperature at 15 mbar. At 15°S, the difference of temperature between the nominal retrieval and the retrieval with the methane abundance retrieved by Lellouch et al. (2014) ($q_{\text{CH}_4} = 0.95\%$), is approximately 9 K on the whole pressure range.

We performed additional temperature retrievals using CIRS FP4 nadir spectra measured at the same times and latitudes as the two datasets shown in Fig. 3. In FP4 nadir spectra, the methane band ν_4 is visible between 1200 cm⁻¹ and 1360 cm⁻¹. This spectral feature allows us to probe temperature between 0.1 mbar and 10 mbar, whereas methane rotational lines in the CIRS FP1 nadir spectra generally probe temperature between 6 mbar and 25 mbar. Temperature can thus be measured with both types of retrievals from 6 mbar to 10 mbar. We performed FP4 temperature retrievals with the nominal methane abundance and the abundances measured by Lellouch et al. (2014), as shown in Fig. 3. FP4 temperature retrievals seem less sensitive to changes in the methane volume mixing ratio, as they yield a maximal temperature difference of 3 K at 52°N, and 4 K at 15°S between 6 mbar

and 10 mbar. In both cases, FP1 and FP4 temperature retrievals are in better agreement in their common pressure range when the nominal methane abundance ($q_{\text{CH}_4} = 1.48\%$) is used for both retrievals. This suggests that $q_{\text{CH}_4} = 1.48\%$ is the best choice, at least in the pressure range covered by both types of temperature retrievals (from 6 mbar to 10 mbar). Changing the abundance of CH₄ in the whole stratosphere seems to induce an error on the temperature measurements between 6 mbar and 10 mbar (up to 9 K at 15°S), which probably affects the temperature at 15 mbar in the FP1 retrievals, because of the vertical resolution of nadir retrievals (represented by the width of the inversion kernels in Fig. 2). Consequently, assessing the effects of CH₄ abundance variations on temperature at 15 mbar by changing q_{CH_4} in the whole stratosphere seems to be a very unfavourable test, and the uncertainties on temperature determined by this method are probably overestimated for the FP1 temperature retrievals. Overall, when retrieving temperature from CIRS FP1 nadir spectra with $q_{\text{CH}_4} = 1\%$ for datasets spanning different times and latitudes, we found temperatures warmer than our nominal temperatures by 2 K to 10 K at 15 mbar, with an average of 5 K. In Lellouch et al. (2014), authors found that temperature changes by 4–5 K on the whole pressure range when varying q_{CH_4} at 15°S, but they determined temperatures using FP4 nadir and limb data, which do not probe the 15 mbar pressure level.

3. Results

Figs. 4 and 5 show the temperatures measured with Cassini/CIRS far-IR nadir data at 6 mbar (minimal pressure probed by the CIRS far-IR nadir observations) and 15 mbar (pressure level where these observations are the most sensitive). Fig. 4 maps the seasonal evolution of temperatures throughout the Cassini mission (from 2004 to 2017, i.e. from mid-northern winter to early summer), while Fig. 5 is focused on the evolution of the meridional gradient of temperature from one season to another. In both figures, both pressure levels exhibit significant seasonal variations of temperature and follow similar trends. Maximal temperatures are reached near the equator in 2005 (152 K at 6 mbar, 130 K at 15 mbar, at 18°S, at $L_S = 300^\circ$), while the minimal temperatures are reached at high southern latitudes in autumn (123 K at 6 mbar, 106 K at 15 mbar at 70°S in 2016, at $L_S = 79^\circ$).

The maximal seasonal variations of temperature are located at the poles for both pressure levels. At high northern latitudes (60°N–90°N), at 15 mbar, the temperature increased overall from winter to summer solstice. For instance at 70°N, temperature increased by 10 K from January 2007 to September 2017. At 6 mbar, temperatures at 60°N stayed approximately constant from winter to spring, whereas latitudes poleward from 70°N warmed up. At 85°N, the temperature increased continuously from 125 K in March 2007 to 142 K in September 2017.

In the meantime, at high southern latitudes (60°S–90°S), at 6 mbar and 15 mbar, temperatures strongly decreased from southern summer (2007) to late autumn (2016). It is the largest seasonal temperature change we measured in the lower stratosphere. At 70°S, temperature decreased by 24 K at 6 mbar and by 19 K at 15 mbar between January 2007 and June 2016. This decrease seems to be followed by a temperature increase toward winter solstice. At 70°S, temperatures varied by +8 K at 6 mbar from June 2016 to April 2017. Temperatures at high southern latitudes began to evolve in November 2010 at 6 mbar, and 2 years later (in August 2012) at 15 mbar.

Other latitudes experience moderate seasonal temperature variations. At low latitudes (between 30°N and 30°S), temperature decreased overall from 2004 to 2017 at both pressure levels. For instance, at the equator, at 6 mbar temperature decreased by 6 K from 2006 to 2016. At mid-southern latitudes, temperatures stayed constant from summer (2005) to mid-autumn (June 2012 at 6 mbar, and May 2013 at 15 mbar), then they decreased by approximately 10 K from 2012–2013 to 2016. At mid-northern latitudes temperatures increased overall from winter to spring. At 50°N, temperature increased from 139 K to 144 K from 2005 to 2014. In Fig. 5, at 6 mbar and 15 mbar, the meridional

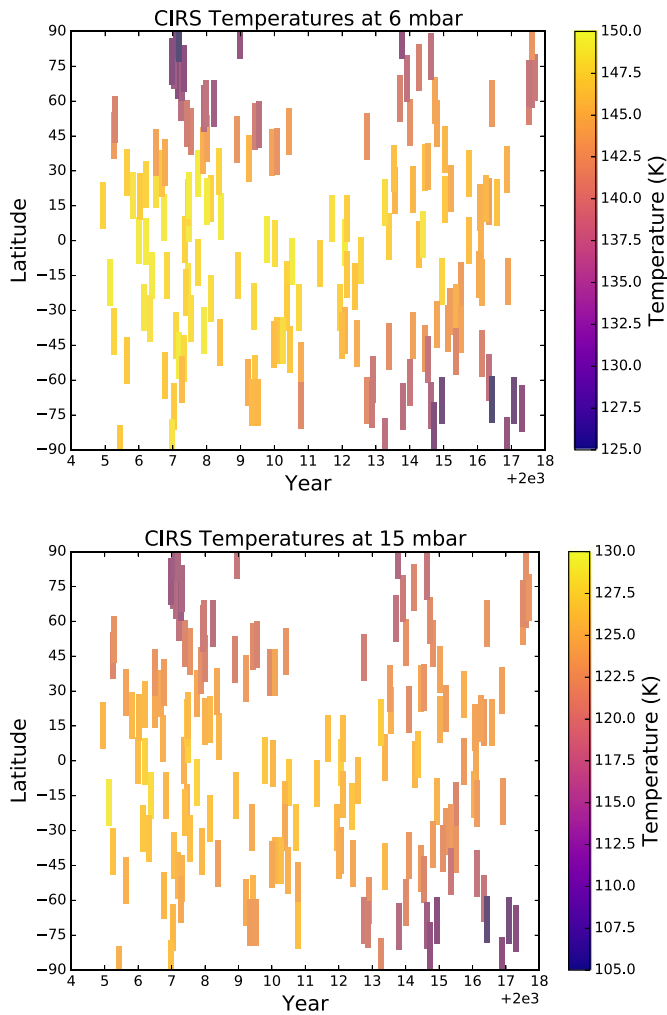


Fig. 4. Evolution of temperatures at 6 mbar (120 km) and 15 mbar (85 km) from northern winter (2004) to summer (2017). The length of the markers shows the average size of the field of view of the CIRS FP1 detector. Temperatures exhibit similar strong seasonal changes at both pressure levels, especially at the poles.

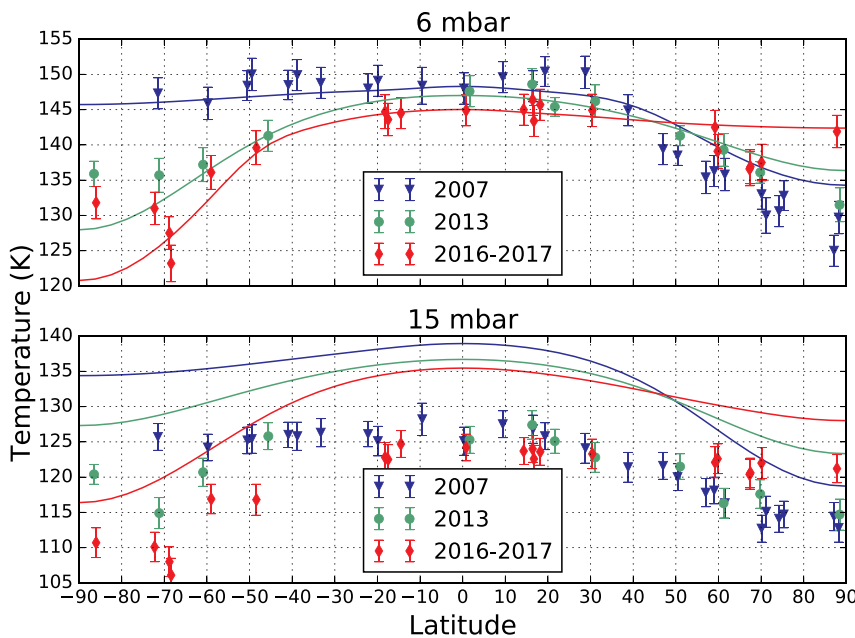


Fig. 5. Meridional distribution of temperatures at 6 mbar (120 km) and 15 mbar (85 km), for three different seasons: late northern winter (2007, blue triangles), mid-spring (2013, green circles), and near summer solstice (from July 2016 to September 2017, red diamonds). The plain lines are the meridional distributions given by GCM simulations at comparable seasons (see Section 4). In both observations and model the meridional gradient of temperatures evolves from one season to another at both pressure levels. (For interpretation of the references to color in this figure legend, the reader is referred to the web version of this article.)

temperature gradient evolves from one season to another. During late northern winter, temperatures were approximately constant from 70°S to 30°N, and then decreased toward the North Pole. In mid-spring, temperatures were decreasing from equator to poles. Near the summer solstice, at 15 mbar, the meridional temperature gradient reversed compared to winter (summer temperatures constant in northern and low southern latitudes then decreasing toward the South Pole), while at 6 mbar, temperatures globally decrease from the equator to the South Pole and 70°N, then increase slightly between 70°N and 90°N. At 15 mbar, most of these changes in the shape of the temperature distribution occur because of the temperature variations poleward from 60°. At 6 mbar, temperature variations occur mostly in the southern hemisphere at latitudes higher than 40°S, and near the North Pole at latitudes higher than 70°N.

Fig. 6 shows the first and the last temperature profiles measured with CIRS nadir far-IR data, for several latitudes. As in Fig. 4, the maximal temperature variations are measured at high southern latitudes for all pressure levels. At 70°S, the temperature decreased by 25 K at 10 mbar. Below 10 mbar the seasonal temperature difference decreases rapidly with increasing pressure until it reaches 10 K at 25 mbar, whereas it is nearly constant between 5 mbar and 10 mbar. 85°N also exhibits a decrease of the seasonal temperature gradient below the 10 mbar pressure level, although it is less pronounced than near the South Pole. At 45°S, the temperature decreased by approximately 10 K from 2007 to 2016, over the whole probed pressure range. At the equator, the temperature varies by -5 K from 2005 to 2016 at 6 mbar and the amplitude of this variation seems to decrease slightly with increasing pressure until it becomes negligible at 25 mbar. However the amplitude of these variations is in the same range as the uncertainty on temperature due to potential CH₄ variations.

4. Discussion

4.1. Comparison with previous results

Fig. 7 shows a comparison between our results and previous studies where temperatures have been measured in the lower stratosphere at similar epochs, latitudes and pressure levels. In the top left and right panels, our temperature measurements are compared to results from CIRS FP4 nadir observations (Bampasidis et al., 2012; Coustenis et al., 2016) which probe mainly the 0.1–10 mbar pressure range. In the top

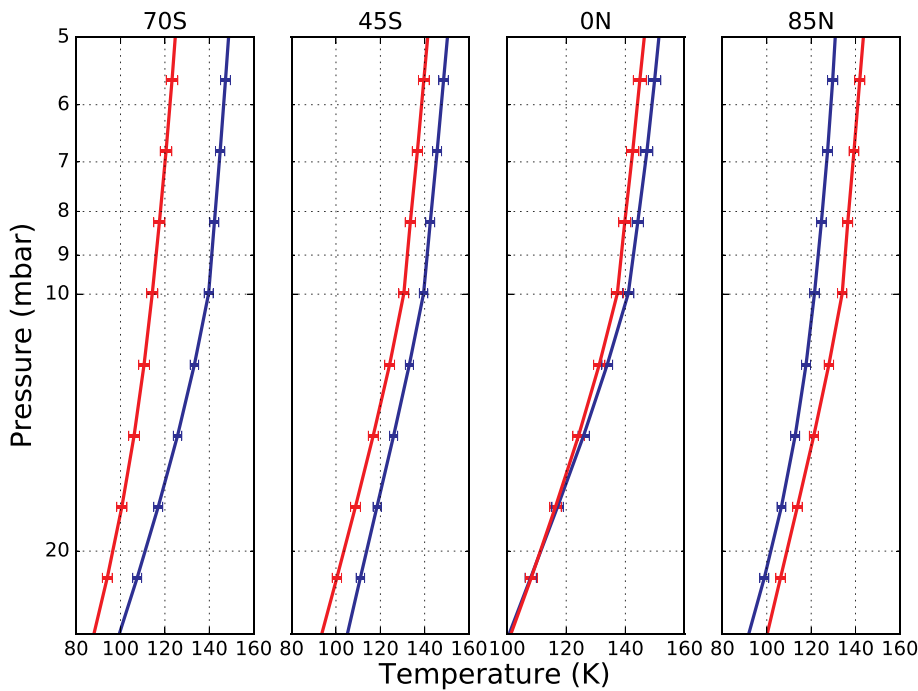


Fig. 6. Temperature variations in the lower stratosphere during the Cassini mission for different latitudes. The blue profiles were measured during northern winter (in 2007). The red profiles were measured in late northern spring (in 2017 for 85°N, in 2016 for the other latitudes). The seasonal temperature variations are observed at most latitudes, and on the whole probed pressure range. (For interpretation of the references to color in this figure legend, the reader is referred to the web version of this article.)

left panel, the temperatures measured at 6 mbar by these two types of observations are in good agreement for the two considered epochs (2009–2010 and 2014). We obtain similar meridional gradients with both types of observations, even if FP4 temperatures are obtained from averages of spectra over bins of 10° of latitudes (except at 70°N and 70°S where the bins are 20° wide in latitude), whereas the average size in latitude of the field of view of the FP1 detector is 20°. It thus seems that the wider latitudinal size of the FP1 field of view has little effect on

our temperature measurements. In the right panel, our temperature profiles are compared to two profiles measured by Coustenis et al. (2016) using CIRS FP4 nadir observations (at 50°S in April 2010, and at 70°S in June 2012), and with Cassini radio-occultation measurements from Schinder et al. (2011, 2012), which probe the atmosphere from the surface to 0.1 mbar (0–300 km). CIRS FP1 and FP4 temperature profiles are in good overall agreement. The profile we measured at 28°S in February 2006 and the corresponding radio-occultation profile are

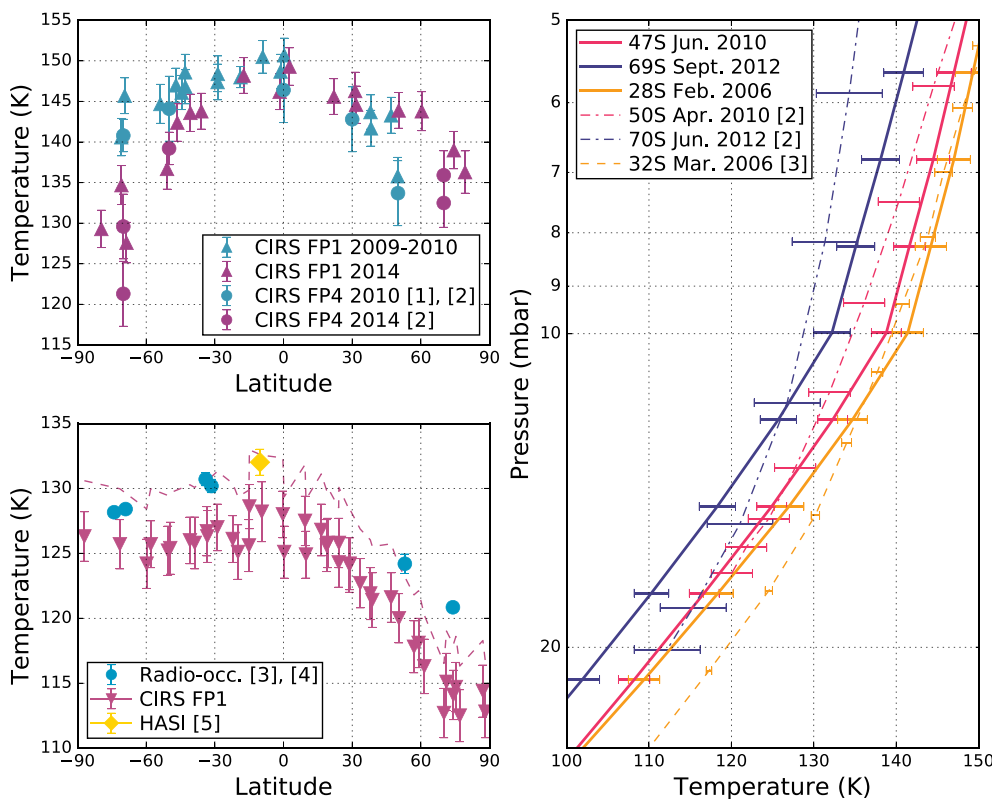


Fig. 7. Comparison of nadir FP1 temperatures with previous studies. Top left panel: Comparison between CIRS nadir FP1 (triangles) and CIRS nadir FP4 temperatures at 6 mbar (circles, Bampasidis et al., 2012 [1], and Coustenis et al., 2016 [2]) in 2010 (cyan) and 2014 (purple). Right panel: Comparison between temperature profiles from CIRS nadir FP1 observations (thick solid lines), CIRS nadir FP4 observations (thin dot-dashed lines, Coustenis et al., 2016 [2]), and Cassini radio-occultation (thin dashed line, Schinder et al., 2011 [3]). Our results are in good agreement with CIRS FP4 temperatures, but diverge somewhat from radio-occultation profiles with increasing pressure. Bottom left panel: Comparison between temperatures at 15 mbar from our CIRS FP1 nadir measurements (magenta triangles), Cassini radio-occultations in 2006 and 2007 (cyan circles, Schinder et al., 2011, 2012, [3], [4]), and the Huygens/HASI measurement in 2005 (yellow diamond, Fulchignoni et al., 2005, [5]). The dashed magenta line shows the potential effect of the CH₄ variations observed by Lellouch et al. (2014). If we take into account this effect, the agreement between our data, the radio-occultations and the HASI measurements is good. (For interpretation of the references to color in this figure legend, the reader is referred to the web version of this article.)

within error bars for pressures lower than 13 mbar, then the difference between them increases up to 8 K at 25 mbar. The bottom left panel of Fig. 7 shows the radio-occultation temperatures in 2006 and 2007 compared to CIRS nadir FP1 temperatures at 15 mbar, where their sensitivity to the temperature is maximal. Although, the radio-occultations temperatures are systematically higher than the CIRS temperatures by 2 K to 6 K, they follow the same meridional trend. CIRS FP1 temperatures at the equator are also lower than the temperature measured by the HASI instrument at 15 mbar during Huygens descent in Titan's atmosphere in 2005. If we take into account the effect of the spatial variations of CH₄ at 15 mbar observed by Lellouch et al. (2014) by decreasing the CH₄ abundance to 1% (the lower limit in Lellouch et al., 2014) in the CIRS FP1 temperature measurements (dashed line in the middle panel of Fig. 7), the agreement between the three types of observations is good in the southern hemisphere. The differences between radio-occultations, HASI and CIRS temperatures might also be explained by the difference of vertical resolution. Indeed, nadir observations have a vertical resolution in the order of 50 km while radio-occultations and HASI observations have respective vertical resolutions of 1 km and 200 m around 15 mbar.

4.2. Effects of Saturn's eccentricity

Because of Saturn's orbital eccentricity of 0.0565, the distance between Titan and the Sun varies enough to affect significantly the insolation. For instance, throughout the Cassini mission, the solar flux received at the equator has decreased by 19% because of the eccentricity. We make a simple model of the evolution of the temperature T at the equator as a function of the distance between Titan and the Sun. In this model we assume that the temperature T at the considered pressure level and at a given time depends **only on** the absorbed solar flux F and we neglect the radiative exchanges between atmospheric layers:

$$\epsilon\sigma T^4 = F \quad (2)$$

where ϵ is the emissivity of the atmosphere at this pressure level, and σ the Stefan-Boltzmann constant. T can thus be defined as a function of the distance d between Titan and the Sun:

$$T^4 = \frac{\alpha L_{\odot}}{16\epsilon\sigma\pi d^2} \quad (3)$$

where L_{\odot} is the solar power, and α the absorptivity of the atmosphere. If we choose a reference temperature T_0 where Titan is at a distance d_0 from the Sun, a relation similar to Eq. (3) can be written for T_0 . If we assume ϵ and α to be constant, T can then be written as:

$$T = T_0 \sqrt{\frac{d_0}{d}} \quad (4)$$

Fig. 8 shows a comparison between this model and the temperatures measured between 5°N and 5°S from 2006 to 2016, at 6 mbar and 15 mbar. We choose T_0 as the temperature at the beginning of the observations (December 2005/January 2006) which provides the best fit between our model and the observations while being consistent with the observations at the same epoch ($T_0 = 151.7$ K at 6 mbar, and $T_0 = 129$ K at 15 mbar). At 6 mbar, we measure a temperature decrease from 2006 to 2016. This is similar to what has been measured at 4 mbar by Bézard et al. (2018) with CIRS mid-IR observations, whereas their radiative-dynamical model predicts a small temperature maximum around the northern spring equinox (2009). At 15 mbar, equatorial temperatures are mostly constant from 2005 to 2016, with a marginal decrease in 2016. Our model predicts temperature variations of 8 K at 6 mbar and 7 K at 15 mbar from 2006 to 2016. Both predictions are consistent with the measurements and with radiative timescales shorter than one Titan year at 6 mbar and 15 mbar, as in Bézard et al. (2018) where they are respectively equal to 0.024 Titan year and 0.06 Titan year. At both pressure levels, the model captures the magnitude of the

temperature change, but does not fully match its timing or shape (especially in 2012–2014), implying that a more sophisticated model is needed. The remaining differences between our model and the temperature measurements could be decreased by adding a temporal lag to our model (2–3 years at 6 mbar and 3–4 years at 15 mbar), but the error bars on the temperature measurements are too large to constrain the lag to a value statistically distinct from zero. Even with this potential lag, the agreement between the model and the temperatures measured at 6 mbar show that the amplitude of the temporal evolution throughout the Cassini mission may be explained by the effects of Saturn's eccentricity. At 15 mbar, given the error bars and the lack of further far-IR temperature measurements at the equator in 2016 and 2017, it remains difficult to draw a definitive conclusion about the influence of Saturn's eccentricity at this pressure level.

4.3. Implication for radiative and dynamical processes of the lower stratosphere

In Section 3, we showed that in the lower stratosphere, the seasonal evolution of the temperature is maximal at high latitudes, especially at the South Pole. At 15 mbar, the strong cooling of high southern latitudes started in 2012, simultaneously with the increase in C₂N₂, C₄H₂, and C₃H₄ abundances measured at the same latitudes and pressure-level in Sylvestre et al. (2018). We also show that this cooling affects the atmosphere at least down to the 25 mbar pressure level (altitude of 70 km). The enrichment of the gases and cooling are consistent with the onset of a subsidence above the South Pole during autumn, as predicted by GCMs (Newman et al., 2011; Lebonnois et al., 2012), and inferred from previous CIRS observations at higher altitudes (Teanby et al., 2012; Vinatier et al., 2015; Coustenis et al., 2016). As Titan's atmospheric circulation transitions from two equator-to-poles cells (with upwelling above the equator and subsidence above the poles) to a single pole-to-pole cell (with a descending branch above South Pole), this subsidence drags downward photochemical species created at higher altitudes toward the lower stratosphere. Teanby et al. (2017) showed that enrichment in trace gases may be so strong that their cooling effect combined with the insolation decrease may exceed the adiabatic heating between 0.3 mbar and 10 mbar (100–250 km). Our observations show that this phenomena may be at play down as deep as 25 mbar.

We compare retrieved temperature fields with results of simulations from IPSL 3D-GCM (Lebonnois et al., 2012) with an updated radiative transfer scheme (Vatant d'Ollone et al., 2017) now based on a flexible *correlated-k* method and up-to-date gas spectroscopic data (Rothman et al., 2013). It does not take into account the radiative feedback of the enrichment in hazes and trace gases in the polar regions, but it nevertheless appears that there is a good agreement in terms of seasonal cycle between the model and the observations. As shown in Fig. 5, at 6 mbar meridional distributions and values of temperatures in the model match well the observations. It can be pointed out that in both model and observations there is a noticeable asymmetry between high southern latitudes where the temperature decreases rapidly from the equinox to winter, and high northern latitudes which evolve more slowly from winter to summer. For instance, in both CIRS data and model, between 2007 and 2013 at 6 mbar and 70°N the atmosphere has warmed by only about 2 K, while in the meantime at 70°S it has cooled by about 10–15 K. This is consistent with an increase of radiative timescales at high northern latitudes (due to lower temperatures, Achterberg et al., 2011) which would remain cold for approximately one season even after the return of sunlight. Fig. 9 shows the temporal evolution of the temperature at 70°N over one Titan year in the lower stratosphere in the GCM simulations and also emphasizes this asymmetry between the ingress and egress of winter at high latitudes. In Fig. 5, at 15 mbar modeled temperatures underestimate the observations by roughly 5–10 K, certainly due to a lack of infrared coolers such as clouds condensates (Jennings et al., 2015). However, observations and

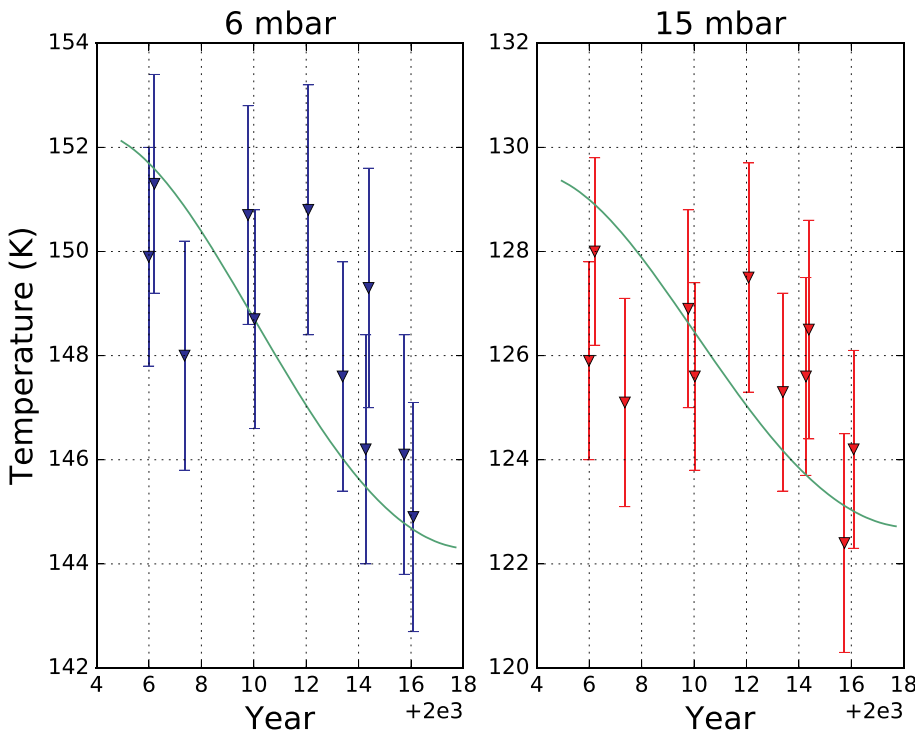


Fig. 8. Temporal evolution of Titan's lower stratospheric temperatures at the equator ($5^{\circ}\text{N} - 5^{\circ}\text{S}$) at 6 mbar (left panel) and 15 mbar (right panel), compared with a simple model of the evolution of the temperature as a function of the distance between Titan and the Sun (green line). The reduced χ^2 between this model and the observations is 0.95 at 6 mbar and 1.07 at 15 mbar. The amplitude of the temperature variations at Titan's equator throughout the Cassini mission can be explained by the effect of Saturn's eccentricity. (For interpretation of the references to color in this figure legend, the reader is referred to the web version of this article.)

simulations exhibit similar meridional temperature gradients for the three studied epochs, and similar seasonal temperature evolution. For instance, in 2016–2017 we measured a temperature gradient of -11 K between the North and South Pole, whereas GCM simulations predict a temperature gradient of -12 K . At 70°S , temperature decreases by 10 K

between 2007 and 2016–2017 in the GCM and in our observations. Besides, at 15 mbar, the seasonal behaviour remains the same as at 6 mbar, although more damped. Indeed comparison with GCM results also supports the idea that the seasonal effects due to the variations of insolation are damped with increasing depth in the lower stratosphere

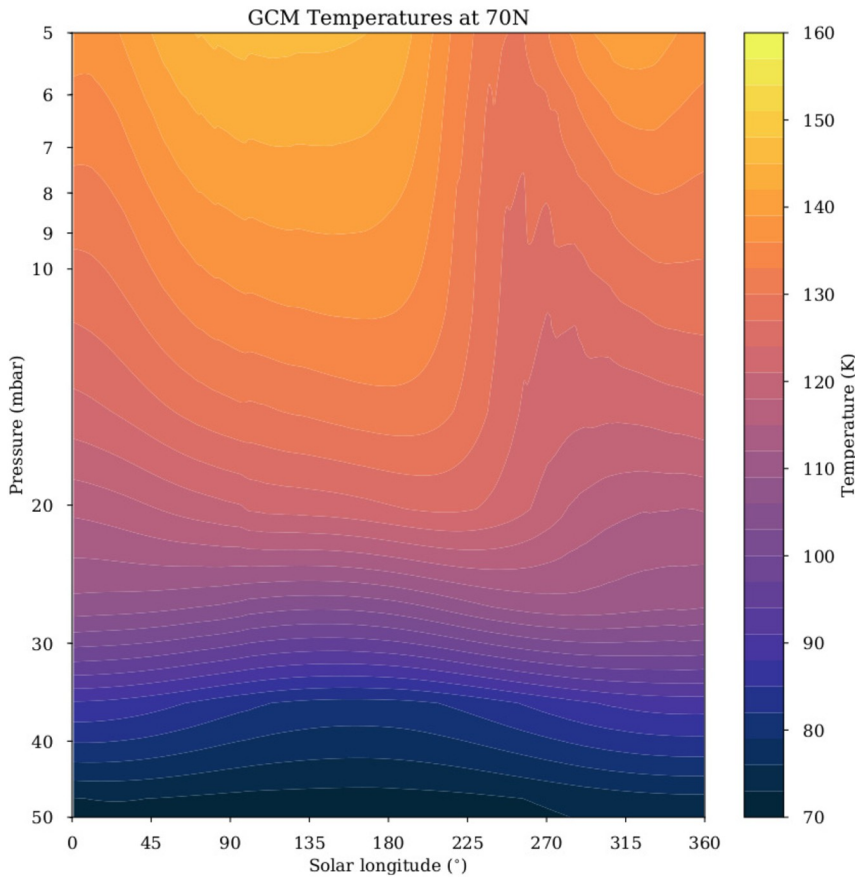


Fig. 9. Seasonal evolution of Titan's lower stratospheric temperatures modeled by the IPSL 3D-GCM at 70°N — between 5 mbar and 50 mbar, starting at northern spring equinox. In the pressure range probed by the CIRS far-IR observations (from 6 mbar to 25 mbar), there is a strong asymmetry between the rapid temperature changes after autumn equinox ($L_S = 180^{\circ}$) and the slow evolution of the thermal structure after spring equinox ($L_S = 0^{\circ}$).

and ultimately muted below 25 mbar, as displayed in Fig. 9. At lower altitudes the seasonal cycle of temperature at high latitudes is even inverted with temperatures increasing in the winter and decreasing in summer. Indeed at these altitudes, due to the radiative timescales exceeding one Titan year, temperature is no more sensitive to the seasonal variations of solar forcing, but to the interplay of ascending and descending large scale vertical motions of the pole-to-pole cell, inducing respectively adiabatic heating above winter pole and cooling above summer pole, as previously discussed in Lebonnois et al. (2012).

Further analysis of simulations – not presented here – also show that after 2016, temperatures at high southern latitudes began to slightly increase again at 6 mbar, which is consistent with observations, whereas at 15 mbar no change in the trend is observed, certainly due to a phase shift of the seasonal cycle between the two altitudes induced by the difference of radiative timescales, which is also illustrated in Fig. 9.

We also show in Fig. 6 that at high southern latitudes, from 6 to 10 mbar seasonal temperature variations are approximately constant with pressure and can be larger than 10 K, whereas they decrease with increasing pressure below 10 mbar. This transition at 10 mbar may be caused by the increase of radiative timescales in the lower stratosphere. Strobel et al. (2010) estimated that the radiative timescale increases from one Titan season at 6 mbar to half a Titan year at 12 mbar. It can thus be expected that this region should be a transition zone between regions of the atmosphere where the atmospheric response to the seasonal insolation variations is significant and comes with little lag, to regions of the atmosphere where they are negligible. However, this transition should be observable at other latitudes such as 45°S, whereas Fig. 6 shows a seasonal gradient constant with pressure at this latitude. Furthermore, in Bézard et al. (2018), the authors show that the method used to estimate radiative timescales in Strobel et al. (2010) tends to overestimate them, and that in their model radiative timescales are less than a Titan season down to the 35 mbar pressure level, which is more consistent with the seasonal variations measured at 45°S.

The 10 mbar transition can also be caused by the interplay between photochemical, radiative and dynamical processes at high latitudes. Indeed, as photochemical species are transported downward by the subsidence above the autumn/winter pole, build up and cool strongly the lower atmosphere, the condensation level of species such as HCN, HC₃N, C₄H₂ or C₆H₆ may be shifted upward, toward the 10 mbar level. Hence, below this pressure level, the volume mixing ratios of these gases would rapidly decrease, along with their cooling effect. Many observations, especially during the Cassini mission showed that during winter and autumn, polar regions host clouds composed of ices of photochemical species. For instance, the “haystack” feature showed in Fig. 1 has been studied at both poles in Coustenis et al. (1999), Jennings et al. (2012, 2015), and is attributed to a mixture of condensates, possibly of nitrile origin. Moreover, HCN ice has been measured in the southern polar cloud observed by de Kok et al. (2014) with Cassini/

VIMS observations. C₆H₆ ice has also been detected by Vinatier et al. (2018) in CIRS observations of the South Pole. The condensation curve for C₄H₂ in Barth (2017) is also consistent with the formation of C₄H₂ ice around 10 mbar with the temperatures we measured at 70°S in 2016. These organic ices may also have a cooling effect themselves as Bézard et al. (2018) showed that at 9 mbar, the nitrile haze measured by Anderson and Samuelson (2011) contributes to the cooling with an intensity comparable to the contribution of gases such as C₂H₂ and C₂H₆.

5. Conclusion

In this paper, we analysed all the available nadir far-IR CIRS observations to measure Titan's lower stratospheric temperatures (6 mbar–25 mbar) throughout the 13 years of the Cassini mission, from northern winter to summer solstice. In this pressure range, significant temperature changes occur from one season to another. Temperatures evolve moderately at low and mid-latitudes (less than 10 K between 6 and 15 mbar). At the equator, at 6 mbar we measure a temperature decrease mostly due to Saturn's eccentricity. Seasonal temperature changes are maximal at high latitudes, especially in the southern hemisphere where they reach up to –19 K at 70°S between summer (2007) and late autumn (2016) at 15 mbar. The strong seasonal evolution of high southern latitudes is due to a complex interplay between photochemistry, atmospheric dynamics with the downwelling above the autumn/winter poles, radiative processes with a large contribution of the gases transported toward the lower stratosphere, and possibly condensation due to the cold autumn polar temperatures and strong enrichments in trace gases.

Recent GCM simulations show a good agreement with the observed seasonal variations in this pressure range, even though these simulations do not include coupling with variations of opacity sources. In particular at high latitudes, the fast decrease of temperatures when entering winter and slower increase when getting into summer is well reproduced in these simulations.

Acknowledgements

This research was funded by the UK Science and Technology Facilities Council (grant number ST/M007715/1) and the Cassini project. JVO and SL acknowledge support from the Centre National d'Études Spatiales (CNES). GCM simulations have been performed thanks to computation facilities provided by the Grand Équipement National de Calcul Intensif (GENCI) on the Occigen/CINES cluster (allocation A0040110391). This research made use of Astropy, a community-developed core Python package for Astronomy (Astropy Collaboration et al., 2013), and matplotlib, a Python library for publication quality graphics (Hunter, 2007)

Appendix A. Cassini/CIRS datasets analysed in this study

Table 1

Far-IR CIRS datasets presented in this study. N stands for the number of spectra measured during the acquisition. FOV is the field of view. The asterisk denotes datasets where two different latitudes were observed.

Observations	Date	N	Latitude (°N)	FOV (°)
CIRS_00BTI_FIRNADCMP001_PRIME	12 Dec. 2004	224	16.4	20.3
CIRS_003TI_FIRNADCMP002_PRIME	15 Feb. 2005	180	–18.7	18.5
CIRS_005TI_FIRNADCMP002_PRIME	31 Mar. 2005	241	–41.1	25.7
CIRS_005TI_FIRNADCMP003_PRIME	01 Apr. 2005	240	47.8	28.5
CIRS_006TI_FIRNADCMP002_PRIME	16 Apr. 2005	178	54.7	29.9
CIRS_009TI_COMPMP002_PRIME	06 Jun. 2005	184	–89.7	21.1
CIRS_013TI_FIRNADCMP003_PRIME	21 Aug. 2005	192	30.1	15.5
CIRS_013TI_FIRNADCMP004_PRIME	22 Aug. 2005	248	–53.7	25.0
CIRS_017TI_FIRNADCMP003_PRIME	28 Oct. 2005	119	20.1	19.8
CIRS_019TI_FIRNADCMP002_PRIME	26 Dec. 2005	124	–0.0	17.6

(continued on next page)

Table 1 (continued)

Observations	Date	N	Latitude (°N)	FOV (°)
CIRS_020TI_FIRNADCMP002_PRIME	14 Jan. 2006	107	19.5	19.7
CIRS_021TI_FIRNADCMP002_PRIME	27 Feb. 2006	213	-30.2	22.5
CIRS_022TI_FIRNADCMP003_PRIME	18 Mar. 2006	401	-0.4	18.4
CIRS_022TI_FIRNADCMP008_PRIME	19 Mar. 2006	83	25.3	24.1
CIRS_023TI_FIRNADCMP002_PRIME	01 May 2006	215	-35.0	27.8
CIRS_024TI_FIRNADCMP003_PRIME	19 May 2006	350	-15.5	21.6
CIRS_025TI_FIRNADCMP002_PRIME	02 Jul. 2006	307	25.1	21.7
CIRS_025TI_FIRNADCMP003_PRIME	01 Jul. 2006	190	39.7	25.6
CIRS_028TI_FIRNADCMP003_PRIME	07 Sep. 2006	350	29.7	19.7
CIRS_029TI_FIRNADCMP003_PRIME	23 Sep. 2006	312	9.5	19.4
CIRS_030TI_FIRNADCMP002_PRIME	10 Oct. 2006	340	-59.1	23.4
CIRS_030TI_FIRNADCMP003_PRIME	09 Oct. 2006	286	33.9	19.9
CIRS_031TI_COMPMAP001_VIMS	25 Oct. 2006	160	-14.5	16.3
CIRS_036TI_FIRNADCMP002_PRIME	28 Dec. 2006	136	-89.1	12.6
CIRS_036TI_FIRNADCMP003_PRIME	27 Dec. 2006	321	78.6	21.0
CIRS_037TI_FIRNADCMP001_PRIME	12 Jan. 2007	161	75.2	19.1
CIRS_037TI_FIRNADCMP002_PRIME	13 Jan. 2007	107	-70.3	20.6
CIRS_038TI_FIRNADCMP001_PRIME	28 Jan. 2007	254	86.3	16.7
CIRS_038TI_FIRNADCMP002_PRIME	29 Jan. 2007	254	-39.7	22.0
CIRS_039TI_FIRNADCMP002_PRIME	22 Feb. 2007	23	69.9	21.2
CIRS_040TI_FIRNADCMP001_PRIME	09 Mar. 2007	159	-49.2	21.1
CIRS_040TI_FIRNADCMP002_PRIME	10 Mar. 2007	109	88.8	13.3
CIRS_041TI_FIRNADCMP002_PRIME	26 Mar. 2007	102	61.2	19.3
CIRS_042TI_FIRNADCMP001_PRIME	10 Apr. 2007	103	-60.8	26.0
CIRS_042TI_FIRNADCMP002_PRIME	11 Apr. 2007	272	71.5	22.6
CIRS_043TI_FIRNADCMP001_PRIME	26 Apr. 2007	263	-51.4	24.7
CIRS_043TI_FIRNADCMP002_PRIME	27 Apr. 2007	104	77.1	20.0
CIRS_044TI_FIRNADCMP002_PRIME	13 May 2007	104	-0.5	18.8
CIRS_045TI_FIRNADCMP001_PRIME	28 May 2007	231	-22.3	22.6
CIRS_045TI_FIRNADCMP002_PRIME	29 May 2007	346	52.4	29.5
CIRS_046TI_FIRNADCMP001_PRIME	13 Jun. 2007	60	17.6	28.6
CIRS_046TI_FIRNADCMP002_PRIME	14 Jun. 2007	102	-20.8	19.0
CIRS_047TI_FIRNADCMP001_PRIME	29 Jun. 2007	204	9.8	23.2
CIRS_047TI_FIRNADCMP002_PRIME	30 Jun. 2007	238	20.1	23.7
CIRS_048TI_FIRNADCMP001_PRIME	18 Jul. 2007	96	-34.8	31.4
CIRS_048TI_FIRNADCMP002_PRIME	19 Jul. 2007	260	49.5	35.8
CIRS_050TI_FIRNADCMP001_PRIME	01 Oct. 2007	144	-10.1	23.8
CIRS_050TI_FIRNADCMP002_PRIME	02 Oct. 2007	106	29.9	19.7
CIRS_052TI_FIRNADCMP002_PRIME	19 Nov. 2007	272	40.3	26.5
CIRS_053TI_FIRNADCMP001_PRIME	04 Dec. 2007	223	-40.2	25.8
CIRS_053TI_FIRNADCMP002_PRIME	05 Dec. 2007	102	59.4	28.3
CIRS_054TI_FIRNADCMP002_PRIME	21 Dec. 2007	107	60.4	21.1
CIRS_055TI_FIRNADCMP001_PRIME	05 Jan. 2008	190	18.7	30.5
CIRS_055TI_FIRNADCMP002_PRIME	06 Jan. 2008	284	44.6	22.2
CIRS_059TI_FIRNADCMP001_PRIME	22 Feb. 2008	172	-24.9	20.7
CIRS_059TI_FIRNADCMP002_PRIME	23 Feb. 2008	98	17.1	20.0
CIRS_062TI_FIRNADCMP002_PRIME	25 Mar. 2008	115	59.3	17.1
CIRS_067TI_FIRNADCMP002_PRIME	12 May 2008	286	29.5	21.0
CIRS_069TI_FIRNADCMP001_PRIME	27 May 2008	112	-44.6	27.3
CIRS_069TI_FIRNADCMP002_PRIME	28 May 2008	112	9.5	19.3
CIRS_093TI_FIRNADCMP002_PRIME	20 Nov. 2008	161	43.7	21.1
CIRS_095TI_FIRNADCMP001_PRIME	05 Dec. 2008	213	-14.0	20.7
CIRS_097TI_FIRNADCMP001_PRIME	20 Dec. 2008	231	-10.9	23.7
CIRS_106TI_FIRNADCMP001_PRIME	26 Mar. 2009	165	-60.3	19.2
CIRS_107TI_FIRNADCMP002_PRIME	27 Mar. 2009	164	33.5	30.4
CIRS_110TI_FIRNADCMP001_PRIME	06 May 2009	282	-68.1	25.7
CIRS_111TI_FIRNADCMP002_PRIME	22 May 2009	168	-27.1	23.1
CIRS_112TI_FIRNADCMP001_PRIME	06 Jun. 2009	218	48.7	21.0
CIRS_112TI_FIRNADCMP002_PRIME	07 Jun. 2009	274	-58.9	20.2
CIRS_114TI_FIRNADCMP001_PRIME	09 Jul. 2009	164	-71.4	25.4
CIRS_115TI_FIRNADCMP001_PRIME	24 Jul. 2009	146	50.7	20.1
CIRS_119TI_FIRNADCMP002_PRIME	12 Oct. 2009	166	0.4	18.3
CIRS_122TI_FIRNADCMP001_PRIME	11 Dec. 2009	212	39.8	24.7
CIRS_123TI_FIRNADCMP002_PRIME	28 Dec. 2009	186	-46.1	22.3
CIRS_124TI_FIRNADCMP002_PRIME	13 Jan. 2010	272	-1.2	19.0
CIRS_125TI_FIRNADCMP001_PRIME	28 Jan. 2010	156	39.9	27.5
CIRS_125TI_FIRNADCMP002_PRIME	29 Jan. 2010	280	-44.9	27.3
CIRS_129TI_FIRNADCMP001_PRIME	05 Apr. 2010	119	-45.1	28.2
CIRS_131TI_FIRNADCMP001_PRIME	19 May 2010	188	-30.0	22.1
CIRS_131TI_FIRNADCMP002_PRIME	20 May 2010	229	-19.8	21.5
CIRS_132TI_FIRNADCMP002_PRIME	05 Jun. 2010	167	49.4	27.4
CIRS_133TI_FIRNADCMP001_PRIME	20 Jun. 2010	187	-49.7	36.1
CIRS_134TI_FIRNADCMP001_PRIME	06 Jul. 2010	251	-10.0	20.0
CIRS_138TI_FIRNADCMP001_PRIME	24 Sep. 2010	190	-30.1	21.2

(continued on next page)

Table 1 (continued)

Observations	Date	N	Latitude (°N)	FOV (°)
CIRS_139TI_COMPMPA001_PRIME*	14 Oct. 2010	132	-70.9	20.6
CIRS_139TI_COMPMPA001_PRIME*	14 Oct. 2010	108	-53.8	16.7
CIRS_148TI_FIRNADCMP001_PRIME	08 May 2011	200	-10.0	18.3
CIRS_153TI_FIRNADCMP001_PRIME	11 Sep. 2011	227	9.9	19.0
CIRS_158TI_FIRNADCMP501_PRIME	13 Dec. 2011	369	-29.9	24.7
CIRS_159TI_FIRNADCMP001_PRIME	02 Jan. 2012	275	-42.2	23.7
CIRS_160TI_FIRNADCMP001_PRIME	29 Jan. 2012	322	-40.0	21.7
CIRS_160TI_FIRNADCMP002_PRIME	30 Jan. 2012	280	-0.2	18.3
CIRS_161TI_FIRNADCMP001_PRIME	18 Feb. 2012	121	9.9	18.4
CIRS_161TI_FIRNADCMP002_PRIME	19 Feb. 2012	89	-15.0	17.3
CIRS_166TI_FIRNADCMP001_PRIME	22 May 2012	318	-19.9	19.9
CIRS_167TI_FIRNADCMP002_PRIME	07 Jun. 2012	293	-45.4	21.7
CIRS_169TI_FIRNADCMP001_PRIME	24 Jul. 2012	258	-9.7	20.7
CIRS_172TI_FIRNADCMP001_PRIME	26 Sep. 2012	282	44.9	18.5
CIRS_172TI_FIRNADCMP002_PRIME	26 Sep. 2012	270	-70.4	23.2
CIRS_174TI_FIRNADCMP002_PRIME	13 Nov. 2012	298	-71.8	21.8
CIRS_175TI_FIRNADCMP002_PRIME	29 Nov. 2012	299	-59.9	19.3
CIRS_185TI_FIRNADCMP001_PRIME	05 Apr. 2013	244	15.0	20.1
CIRS_185TI_FIRNADCMP002_PRIME	06 Apr. 2013	303	-88.9	16.8
CIRS_190TI_FIRNADCMP001_PRIME	23 May 2013	224	-0.2	25.6
CIRS_190TI_FIRNADCMP002_PRIME	24 May 2013	298	-45.0	20.0
CIRS_194TI_FIRNADCMP001_PRIME	10 Jul. 2013	186	30.0	19.7
CIRS_195TI_FIRNADCMP001_PRIME	25 Jul. 2013	186	19.6	24.5
CIRS_197TI_FIRNADCMP001_PRIME	11 Sep. 2013	330	60.5	19.4
CIRS_198TI_FIRNADCMP001_PRIME	13 Oct. 2013	187	88.9	8.7
CIRS_198TI_FIRNADCMP002_PRIME	14 Oct. 2013	306	-69.8	24.0
CIRS_199TI_FIRNADCMP001_PRIME	30 Nov. 2013	329	68.4	23.9
CIRS_200TI_FIRNADCMP001_PRIME	01 Jan. 2014	187	49.9	19.6
CIRS_200TI_FIRNADCMP002_PRIME	02 Jan. 2014	210	-59.8	21.3
CIRS_201TI_FIRNADCMP001_PRIME	02 Feb. 2014	329	19.9	26.8
CIRS_201TI_FIRNADCMP002_PRIME	03 Feb. 2014	234	-39.6	20.9
CIRS_203TI_FIRNADCMP001_PRIME	07 Apr. 2014	187	75.0	18.0
CIRS_203TI_FIRNADCMP002_PRIME	07 Apr. 2014	239	0.5	27.5
CIRS_204TI_FIRNADCMP002_PRIME	18 May 2014	199	0.4	27.0
CIRS_205TI_FIRNADCMP001_PRIME	18 Jun. 2014	144	-45.1	20.5
CIRS_205TI_FIRNADCMP002_PRIME	18 Jun. 2014	161	30.3	19.1
CIRS_206TI_FIRNADCMP001_PRIME	19 Jul. 2014	181	-50.3	17.8
CIRS_206TI_FIRNADCMP002_PRIME	20 Jul. 2014	161	30.6	18.4
CIRS_207TI_FIRNADCMP001_PRIME	20 Aug. 2014	179	-70.0	17.8
CIRS_207TI_FIRNADCMP002_PRIME	21 Aug. 2014	163	79.7	17.6
CIRS_208TI_FIRNADCMP001_PRIME	21 Sep. 2014	329	-80.0	15.6
CIRS_208TI_FIRNADCMP002_PRIME	22 Sep. 2014	175	60.5	17.8
CIRS_209TI_FIRNADCMP001_PRIME	23 Oct. 2014	181	-35.2	17.7
CIRS_209TI_FIRNADCMP002_PRIME	24 Oct. 2014	233	50.5	18.5
CIRS_210TI_FIRNADCMP001_PRIME	10 Dec. 2014	329	-70.3	25.2
CIRS_210TI_FIRNADCMP002_PRIME	11 Dec. 2014	237	-19.6	27.6
CIRS_211TI_FIRNADCMP001_PRIME	11 Jan. 2015	225	19.6	25.0
CIRS_211TI_FIRNADCMP002_PRIME	12 Jan. 2015	258	40.0	19.3
CIRS_212TI_FIRNADCMP002_PRIME	13 Feb. 2015	257	-40.0	30.1
CIRS_213TI_FIRNADCMP001_PRIME	16 Mar. 2015	187	-31.6	19.6
CIRS_213TI_FIRNADCMP002_PRIME	16 Mar. 2015	258	23.4	20.5
CIRS_215TI_FIRNADCMP001_PRIME	07 May 2015	250	-50.0	31.0
CIRS_215TI_FIRNADCMP002_PRIME	08 May 2015	232	-30.0	21.7
CIRS_218TI_FIRNADCMP001_PRIME	06 Jul. 2015	249	-20.0	19.9
CIRS_218TI_FIRNADCMP002_PRIME	07 Jul. 2015	232	-40.0	25.2
CIRS_222TI_FIRNADCMP001_PRIME	28 Sep. 2015	125	30.0	21.7
CIRS_222TI_FIRNADCMP002_PRIME	29 Sep. 2015	233	-0.1	18.6
CIRS_230TI_FIRNADCMP001_PRIME	15 Jan. 2016	282	-15.0	19.5
CIRS_231TI_FIRNADCMP001_PRIME	31 Jan. 2016	254	15.0	19.6
CIRS_231TI_FIRNADCMP002_PRIME	01 Feb. 2016	236	0.4	18.9
CIRS_232TI_FIRNADCMP001_PRIME	16 Feb. 2016	249	-50.2	24.5
CIRS_232TI_FIRNADCMP002_PRIME	17 Feb. 2016	92	-19.8	21.5
CIRS_234TI_FIRNADCMP001_PRIME	04 Apr. 2016	328	19.8	24.7
CIRS_235TI_FIRNADCMP001_PRIME	06 May 2016	163	-60.0	19.7
CIRS_235TI_FIRNADCMP002_PRIME	07 May 2016	221	15.7	20.1
CIRS_236TI_FIRNADCMP001_PRIME	07 Jun. 2016	88	-70.5	20.5
CIRS_236TI_FIRNADCMP002_PRIME	07 Jun. 2016	238	60.8	20.0
CIRS_238TI_FIRNADCMP002_PRIME	25 Jul. 2016	220	15.4	20.5
CIRS_248TI_FIRNADCMP001_PRIME	13 Nov. 2016	185	-88.9	18.3
CIRS_248TI_FIRNADCMP002_PRIME	14 Nov. 2016	186	30.3	17.4
CIRS_250TI_FIRNADCMP002_PRIME	30 Nov. 2016	219	-19.8	28.4
CIRS_259TI_COMPMPA001_PIE	01 Feb. 2017	302	-69.0	20.6
CIRS_270TI_FIRNADCMP001_PRIME	21 Apr. 2017	166	-74.7	25.4
CIRS_283TI_COMPMPA001_PRIME*	10 Jul. 2017	114	60.0	26.5

(continued on next page)

Table 1 (continued)

Observations	Date	N	Latitude (°N)	FOV (°)
CIRS_283TI_COMPMPA001_PRIME*	10 Jul. 2017	134	67.5	24.7
CIRS_287TI_COMPMPA001_PIE	11 Aug. 2017	305	88.9	9.3
CIRS_288TI_COMPMPA002_PIE	11 Aug. 2017	269	66.7	23.7
CIRS_292TI_COMPMPA001_PRIME	12 Sep. 2017	192	70.4	19.2

References

- Achterberg, R.K., Conrath, B.J., Gierasch, P.J., Flasar, F.M., Nixon, C.A., 2008. Titan's middle-atmospheric temperatures and dynamics observed by the Cassini Composite Infrared Spectrometer. *Icarus* 194, 263–277 Mar.
- Achterberg, R.K., Gierasch, P.J., Conrath, B.J., Michael Flasar, F., Nixon, C.A., 2011. Temporal variations of Titan's middle-atmospheric temperatures from 2004 to 2009 observed by Cassini/CIRS. *Icarus* 211, 686–698 Jan.
- Anderson, C., Samuelson, R., Achterberg, R., 2012. Titan's stratospheric condensibles at high northern latitudes during northern winter. In: Cottini, V., Nixon, C., Lorenz, R. (Eds.), *Titan Through Time; Unlocking Titan's Past, Present and Future*, pp. 59 Apr.
- Anderson, C.M., Samuelson, R.E., 2011. Titan's aerosol and stratospheric ice opacities between 18 and 500 μm : vertical and spectral characteristics from Cassini CIRS. *Icarus* 212, 762–778 Apr.
- Astropy Collaboration, Robitaille, T.P., Tollerud, E.J., Greenfield, P., Droettboom, M., Bray, E., Aldcroft, T., Davis, M., Ginsburg, A., Price-Whelan, A.M., Kerzendorf, W.E., Conley, A., Crighton, N., Barbary, K., Muna, D., Ferguson, H., Grollier, F., Parikh, M.M., Nair, P.H., Unther, H.M., Deil, C., Woillez, J., Conseil, S., Kramer, R., Turner, J.E.H., Singer, L., Fox, R., Weaver, B.A., Zabalza, V., Edwards, Z.I., Azalee Bostroem, K., Burke, D.J., Casey, A.R., Crawford, S.M., Dencheva, N., Ely, J., Jenness, T., Labrie, K., Lim, P.L., Pierfederici, F., Pontzen, A., Ptak, A., Refsdal, B., Servillat, M., Streicher, O., 2013. Astropy: A community Python package for astronomy. *Astron. Astrophys.* 558 Oct., A33.
- Bampasidis, G., Coustenis, A., Achterberg, R.K., Vinatier, S., Lavvas, P., Nixon, C.A., Jennings, D.E., Teanby, N.A., Flasar, F.M., Carlson, R.C., Moussas, X., Preka-Papadema, P., Romani, P.N., Guandique, E.A., Stamogiorgos, S., 2012. Thermal and chemical structure variations in Titan's stratosphere during the Cassini mission. *Astrophys. J.* 760 Dec., 144.
- Barth, E.L., 2017. Modeling survey of ices in Titan's stratosphere. *Planet. Space Sci.* 137, 20–31 Mar.
- Bézard, B., Vinatier, S., Achterberg, R.K., 2018. Seasonal radiative modeling of Titan's stratospheric temperatures at low latitudes. *Icarus* 302, 437–450 Mar.
- Cottini, V., Nixon, C.A., Jennings, D.E., Anderson, C.M., Gorius, N., Bjoraker, G.L., Coustenis, A., Teanby, N.A., Achterberg, R.K., Bézard, B., de Kok, R., Lellouch, E., Irwin, P.G.J., Flasar, F.M., Bampasidis, G., 2012. Water vapor in Titan's stratosphere from Cassini CIRS far-infrared spectra. *Icarus* 220, 855–862 Aug.
- Coustenis, A., Achterberg, R.K., Conrath, B.J., Jennings, D.E., Marten, A., Gautier, D., Nixon, C.A., Flasar, F.M., Teanby, N.A., Bézard, B., Samuelson, R.E., Carlson, R.C., Lellouch, E., Bjoraker, G.L., Romani, P.N., Taylor, F.W., Irwin, P.G.J., Fouchet, T., Hubert, A., Orton, G.S., Kunde, V.G., Vinatier, S., Mondellini, J., Abbas, M.M., Courtin, R., 2007. The composition of Titan's stratosphere from Cassini/CIRS mid-infrared spectra. *Icarus* 189, 35–62 Jul.
- Coustenis, A., Jennings, D.E., Achterberg, R.K., Bampasidis, G., Lavvas, P., Nixon, C.A., Teanby, N.A., Anderson, C.M., Cottini, V., Flasar, F.M., 2016. Titan's temporal evolution in stratospheric trace gases near the poles. *Icarus* 270, 409–420 May.
- Coustenis, A., Schmitt, B., Khanna, R.K., Trotta, F., 1999. Plausible condensates in Titan's stratosphere from Voyager infrared spectra. *Planet. Space Sci.* 47, 1305–1329 Oct.
- de Kok, R., Irwin, P.G.J., Teanby, N.A., Nixon, C.A., Jennings, D.E., Fletcher, L., Howett, C., Calcutt, S.B., Bowles, N.E., Flasar, F.M., Taylor, F.W., 2007. Characteristics of Titan's stratospheric aerosols and condensate clouds from Cassini CIRS far-infrared spectra. *Icarus* 191, 223–235 Nov.
- de Kok, R., Irwin, P.G.J., Teanby, N.A., Vinatier, S., Tosi, F., Negrão, A., Osprey, S., Adriani, A., Moriconi, M.L., Coradini, A., 2010. A tropical haze band in Titan's stratosphere. *Icarus* 207, 485–490 May.
- de Kok, R.J., Teanby, N.A., Maltagliati, L., Irwin, P.G.J., Vinatier, S., 2014. HCN ice in Titan's high-altitude southern polar cloud. *Nature* 514, 65–67. <https://doi.org/10.1038/nature13789>. Oct.
- Flasar, F.M., Kunde, V.G., Abbas, M.M., Achterberg, R.K., Ade, P., Barucci, A., Bézard, B., Bjoraker, G.L., Brasunas, J.C., Calcutt, S., Carlson, R., Césarsky, C.J., Conrath, B.J., Coradini, A., Courtin, R., Coustenis, A., Edberg, S., Edgington, S., Ferrari, C., Fouchet, T., Gautier, D., Gierasch, P.J., Grossman, K., Irwin, P., Jennings, D.E., Lellouch, E., Mamoutkine, A.A., Marten, A., Meyer, J.P., Nixon, C.A., Orton, G.S., Owen, T.C., Pearl, J.C., Prangé, R., Raulin, F., Read, P.L., Romani, P.N., Samuelson, R.E., Segura, M.E., Showalter, M.R., Simon-Miller, A.A., Smith, M.D., Spencer, J.R., Spilker, L.J., Taylor, F.W., 2004. Exploring the Saturn system in the thermal infrared: the composite infrared spectrometer. *Space Sci. Rev.* 115, 169–297 Dec.
- Fulchignoni, M., Ferri, F., Angrilli, F., Ball, A.J., Bar-Nun, A., Barucci, M.A., Bettanini, C., Bianchini, G., Borucki, W., Colombatti, G., Coradini, M., Coustenis, A., Debei, S., Falkner, P., Fanti, G., Flamini, E., Gaborit, V., Gard, R., Hamelin, M., Harri, A.M., Hath, B., Jernej, I., Leese, M.R., Lehto, A., Lion Stoppato, P.F., López-Moreno, J.J., Mäkinen, T., McDonnell, J.A.M., McKay, C.P., Molina-Cuberos, G., Neubauer, F.M., Pirronello, V., Rodrigo, R., Saggin, B., Schwingschuh, K., Seiff, A., Simões, F., Svedhem, H., Tokano, T., Towner, M.C., Trautner, R., Withers, P., Zarnecki, J.C., 2005. In situ measurements of the physical characteristics of Titan's environment. *Nature* 438, 785–791 Dec.
- Hunter, J.D., 2007. Matplotlib: a 2d graphics environment. *Comput. Sci. Eng.* 9 (3), 90–95.
- Irwin, P.G.J., Teanby, N.A., de Kok, R., Fletcher, L.N., Howett, C.J.A., Tsang, C.C.C., Wilson, C.F., Calcutt, S.B., Nixon, C.A., Parrish, P.D., 2008. The NEMESIS planetary atmosphere radiative transfer and retrieval tool. *J. Quant. Spectrosc. Radiat. Transf.* 109, 1136–1150 Apr.
- Jennings, D.E., Achterberg, R.K., Cottini, V., Anderson, C.M., Flasar, F.M., Nixon, C.A., Bjoraker, G.L., Kunde, V.G., Carlson, R.C., Guandique, E., Kaelberer, M.S., Tingley, J.S., Albright, S.A., Segura, M.E., de Kok, R., Coustenis, A., Vinatier, S., Bampasidis, G., Teanby, N.A., Calcutt, S., 2015. Evolution of the far-infrared cloud at Titan's South Pole. *Astrophys. J. Lett.* 804 May, L34.
- Jennings, D.E., Anderson, C.M., Samuelson, R.E., Flasar, F.M., Nixon, C.A., Kunde, V.G., Achterberg, R.K., Cottini, V., de Kok, R., Coustenis, A., Vinatier, S., Calcutt, S.B., 2012. Seasonal disappearance of far-infrared haze in Titan's stratosphere. *Astrophys. J. Lett.* 754 Jul., L3.
- Lebonnois, S., Burgalat, J., Rannou, P., Charnay, B., 2012. Titan global climate model: a new 3-dimensional version of the IPSL Titan GCM. *Icarus* 218, 707–722 Mar.
- Lellouch, E., Bézard, B., Flasar, F.M., Vinatier, S., Achterberg, R., Nixon, C.A., Bjoraker, G.L., Gorius, N., 2014. The distribution of methane in Titan's stratosphere from Cassini/CIRS observations. *Icarus* 231, 323–337 Mar.
- Lora, J.M., Lunine, J.I., Russell, J.L., 2015. GCM simulations of Titan's middle and lower atmosphere and comparison to observations. *Icarus* 250, 516–528 Apr.
- Maltagliati, L., Bézard, B., Vinatier, S., Hedman, M.M., Lellouch, E., Nicholson, P.D., Sotin, C., de Kok, R.J., Sicardy, B., 2015. Titan's atmosphere as observed by Cassini/VIMS solar occultations: CH₄, CO and evidence for C₂H₆ absorption. *Icarus* 248, 1–24 Mar.
- Molter, E.M., Nixon, C.A., Cordiner, M.A., Serigano, J., Irwin, P.G.J., Teanby, N.A., Charnley, S.B., Lindberg, J.E., 2016. ALMA observations of HCN and its isotopologues on Titan. *Astron. J.* 152 Aug., 42.
- Newman, C.E., Lee, C., Lian, Y., Richardson, M.I., Toigo, A.D., 2011. Stratospheric superrotation in the TitanWRF model. *Icarus* 213, 636–654 Jun.
- Niemann, H.B., Atreya, S.K., Demick, J.E., Gautier, D., Haberman, J.A., Harpold, D.N., Kasprzak, W.T., Lunine, J.I., Owen, T.C., Raulin, F., 2010. Composition of Titan's lower atmosphere and simple surface volatiles as measured by the Cassini-Huygens probe gas chromatograph mass spectrometer experiment. *J. Geophys. Res. Planets* 115 Dec., E12006.
- Nixon, C.A., Temelso, B., Vinatier, S., Teanby, N.A., Bézard, B., Achterberg, R.K., Mandt, K.E., Sherrill, C.D., Irwin, P.G.J., Jennings, D.E., Romani, P.N., Coustenis, A., Flasar, F.M., 2012. Isotopic ratios in Titan's methane: measurements and modeling. *Astrophys. J.* 749 Apr., 159.
- Rothman, L.S., Gordon, L.E., Babikov, Y., Barbe, A., Chris Benner, D., Bernath, P.F., Birk, M., Bizzocchi, L., Boudon, V., Brown, L.R., Campargue, A., Chance, K., Cohen, E.A., Coudert, L.H., Devi, V.M., Drouin, B.J., Fayt, A., Flaud, J.-M., Gamache, R.R., Harrison, J.J., Hartmann, J.-M., Hill, C., Hodges, J.T., Jacquemart, D., Jolly, A., Lamouroux, J., Le Roy, R.J., Li, G., Long, D.A., Lyulin, O.M., Mackie, C.J., Massie, S.T., Mikhailenko, S., Müller, H.S.P., Naumenko, O.V., Nikitin, A.V., Orphal, J., Perevalov, V., Perrin, A., Polovtseva, E.R., Richard, C., Smith, M.A.H., Starikova, E., Sung, K., Tashkun, S., Tennyson, J., Toon, G.C., Tyuterev, V.G., Wagner, G., 2013. The HITRAN2012 molecular spectroscopic database. *J. Quant. Spectrosc. Radiat. Transf.* 130, 4–50 Nov.
- Schinder, P.J., Flasar, F.M., Marouf, E.A., French, R.G., McGhee, C.A., Kliore, A.J., Rappaport, N.J., Barbinis, E., Fleischman, D., Anabtawi, A., 2011. The structure of Titan's atmosphere from Cassini radio occultations. *Icarus* 215, 460–474 Oct.
- Schinder, P.J., Flasar, F.M., Marouf, E.A., French, R.G., McGhee, C.A., Kliore, A.J., Rappaport, N.J., Barbinis, E., Fleischman, D., Anabtawi, A., 2012. The structure of Titan's atmosphere from Cassini radio occultations: occultations from the Prime and Equinox missions. *Icarus* 221, 1020–1031 Nov.
- Strobel, D.F., Atreya, S.K., Bézard, B., Ferri, F., Flasar, F.M., Fulchignoni, M., Lellouch, E., Müller-Wodarg, I., 2010. Atmospheric Structure and Composition. pp. 235.
- Sylvestre, M., Teanby, N.A., Vinatier, S., Lebonnois, S., Irwin, P.G.J., 2018. Seasonal evolution of C₂N₂, C₃H₄, and C₄H₂ abundances in Titan's lower stratosphere. *Astron. Astrophys.* 609 Jan., A64.
- Teanby, N.A., Bézard, B., Vinatier, S., Sylvestre, M., Nixon, C.A., Irwin, P.G.J., de Kok, R.J., Calcutt, S.B., Flasar, F.M., 2017. The formation and evolution of Titan's winter polar vortex. *Nat. Commun.* 8 Nov., 1586.
- Teanby, N.A., Irwin, P.G.J., de Kok, R., Jolly, A., Bézard, B., Nixon, C.A., Calcutt, S.B., 2009, Aug. Titan's stratospheric C₂N₂, C₃H₄, and C₄H₂ abundances from Cassini/CIRS far-infrared spectra. *Icarus* 202, 620–631.
- Teanby, N.A., Irwin, P.G.J., de Kok, R., Vinatier, S., Bézard, B., Nixon, C.A., Flasar, F.M., Calcutt, S.B., Bowles, N.E., Fletcher, L., Howett, C., Taylor, F.W., 2007. Vertical profiles of HCN, HC₃N, and C₂H₂ in Titan's atmosphere derived from Cassini/CIRS

- data. *Icarus* 186, 364–384 Feb.
- Teanby, N.A., Irwin, P.G.J., Nixon, C.A., de Kok, R., Vinatier, S., Coustenis, A., Sefton-Nash, E., Calcutt, S.B., Flasar, F.M., 2012. Active upper-atmosphere chemistry and dynamics from polar circulation reversal on Titan. *Nature* 491, 732–735 Nov.
- Tomasko, M.G., Doose, L., Engel, S., Dafoe, L.E., West, R., Lemmon, M., Karkoschka, E., See, C., 2008. A model of Titan's aerosols based on measurements made inside the atmosphere. *Planet. Space Sci.* 56, 669–707 Apr.
- Vatant d'Ollone, J., Lebonnois, S., Guerlet, S., 2017. Modelling of Titan's middle atmosphere with the IPSL climate model. In: EGU General Assembly Conference Abstracts. vol. 19. pp. 10169 Apr.
- Vinatier, S., Bézard, B., Fouchet, T., Teanby, N.A., de Kok, R., Irwin, P.G.J., Conrath, B.J., Nixon, C.A., Romani, P.N., Flasar, F.M., Coustenis, A., 2007. Vertical abundance profiles of hydrocarbons in Titan's atmosphere at 15°S and 80° N retrieved from Cassini/CIRS spectra. *Icarus* 188, 120–138 May.
- Vinatier, S., Bézard, B., Lebonnois, S., Teanby, N.A., Achterberg, R.K., Gorius, N., Mamoutkine, A., Guandique, E., Jolly, A., Jennings, D.E., Flasar, F.M., 2015. Seasonal variations in Titan's middle atmosphere during the northern spring derived from Cassini/CIRS observations. *Icarus* 250, 95–115 Apr.
- Vinatier, S., Rannou, P., Anderson, C.M., Bézard, B., de Kok, R., Samuelson, R.E., 2012. Optical constants of Titan's stratospheric aerosols in the 70–1500 cm^{-1} spectral range constrained by Cassini/CIRS observations. *Icarus* 219, 5–12 May.
- Vinatier, S., Schmitt, B., Bézard, B., Rannou, P., Dauphin, C., de Kok, R., Jennings, D.E., Flasar, F.M., 2018. Study of Titan's fall southern stratospheric polar cloud composition with Cassini/CIRS: detection of benzene ice. *Icarus* 310, 89–104 Aug.